Multicomponent Nanopatterns by Directed Block Copolymer Self-Assembly

Dong Ok Shin,[†,§,#] Jeong Ho Mun,[†,‡,#] Geon-Tae Hwang,[†] Jong Moon Yoon,[†,‡] Ju Young Kim,[†,‡] Je Moon Yun,[†,‡] Yong-Biao Yang,[⊥] Youngtak Oh,[†,‡] Jeong Yong Lee,[†,‡] Jonghwa Shin,[†] Keon Jae Lee,[†] Soojin Park,[∥] Jaeup U. Kim,[⊥] and Sang Ouk Kim[†,‡,*]

[†]Department of Materials Science and Engineering, Korea Advanced Institute of Science and Tehcnology (KAIST), Daejeon 305-701, Republic of Korea, [‡]Center for Nanomaterials and Chemical Reactions, Institute for Basic Science (IBS), Daejeon 305-701, Republic of Korea, [§]Power Control Device Research Section, Electronics and Telecommunications Research Institute (ETRI), Daejeon 305-700, Republic of Korea, [⊥]School of Mechanical and Advanced Materials Engineering, Ulsan National Institute of Science and Technology (UNIST), Ulsan 689-798, Republic of Korea, and [∥]Interdisciplinary School of Green Energy, Ulsan National Institute of Science and Technology (UNIST), Ulsan 689-798, Republic of Korea. [#]These authors contributed equally to this work.

ABSTRACT Complex nanopatterns integrating diverse nanocomponents are crucial requirements for advanced photonics and electronics. Currently, such multicomponent nanopatterns are principally created by colloidal nanoparticle assembly, where large-area processing of highly ordered nanostructures raises significant challenge. We present multicomponent nanopatterns enabled by block copolymer (BCP) self-assembly, which offers device oriented sub-10-nm scale nanopatterns with arbitrary large-area scalability. In this approach, BCP nanopatterns direct the nanoscale lateral ordering of the overlaid second level BCP nanopatterns to create the superimposed multicomponent nanopatterns incorporating nanowires and nanodots. This approach introduces diverse chemical composition of metallic elements including Au, Pt, Fe, Pd, and Co into sub-10-nm scale nanopatterns. As immediate applications of multicomponent nanopatterns, we demonstrate multilevel charge-trap memory device with Pt—Au binary nanodot pattern and synergistic plasmonic properties of Au nanowire-Pt nanodot pattern.

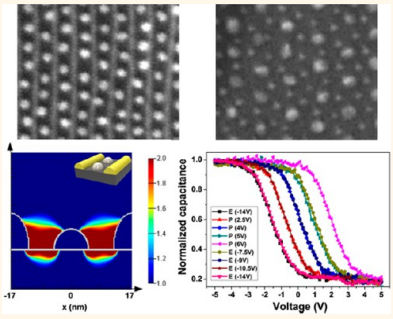

KEYWORDS: multicomponent · nanopattern · block copolymer · self-assembly

Multicomponent nanopatterns, such as binary superlattices, consist of two or more kinds of chemically or morphologically dissimilar nanocomponents.[1−5] Unlike single component counterparts, multicomponent nanopatterns offer enormous diversities in the pattern shape, chemical composition and corresponding functionality. Moreover, synergistic interplay of chemically and morphologically dissimilar nanocomponents may create novel structures and properties, which might inspire the development of advanced photonic and electronic devices. To date, periodic assembly of multiple nanocomponents have principally relied on complex colloidal assembly, which is usually mediated by electrostatic forces[2,6] or biomolecular[7] or other specific interactions.[4] Unfortunately, large-area processing of device oriented structures raises significant challenge in those approaches.[2−7]

Downscaling traditional photolithography below 10 nm scale is suffering from intrinsic optical resolution limit. Numerous alternative or complementary technologies are under development to overcome this major technological challenge. Block copolymer (BCP) self-assembly provides lithography templates for dense sub-10-nm scale features with high-throughput manufacturability, which is hardly attainable by other patterning methods.[8−20] Furthermore, directed self-assembly integrated with conventional photolithography offers laterally ordered device oriented nanopatterns, which holds great promise for cost-effective nanopatterning.[13,14,20−28]

In this work, we introduce BCP self-assembly as an alternative method for multicomponent nanopatterns. Generally, the self-assembled nanopatterns in BCP thin films consist of single-shape monodisperse nanodomains of spheres, cylinders, or lamellae. Therefore, it is hard to integrate multiple nanocomponents. We develop a multilevel approach to address this limitation and successfully generated multicomponent nanopatterns. Our approach is differentiated from

* Address correspondence to sangouk.kim@kaist.ac.kr.

Received for review July 3, 2013 and accepted September 5, 2013.

Published online September 05, 2013
10.1021/nn403379k

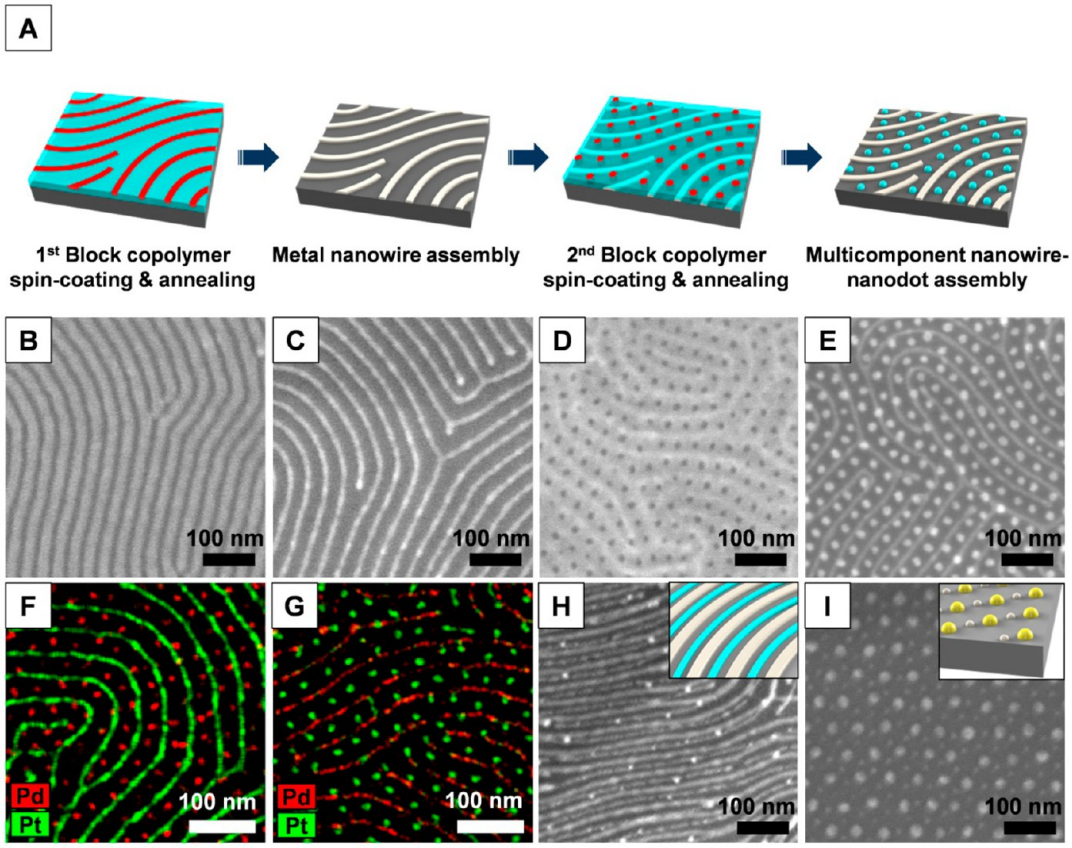

Figure 1. (A) Schematic procedure of multicomponent nanopatterning. (B) The first level BCP self-assembly for surface parallel cylinders. (C) Pt metallization of parallel cylinders. (D) Second level BCP self-assembly for vertical cylinders. (E) Pd metallization of vertical cylinders to complete Pt nanowire–Pd nanodot multicomponent nanopattern. EDS elemental mapping of (F) Pt nanowire–Pd nanodot array and (G) Pd nanowire–Pt nanodot array. Multicomponent nanopatterns of (H) Pt–Pd nanowire array and (I) Au–Pt nanodot array.

the previous approaches relying on complex nanoparticle assembly as follows. The well-established parallel process steps based on BCP self-assembly are genuinely scalable to arbitrary large area processing. In addition, the lateral ordering of multicomponent nanopatterns is precisely controllable by directed self-assembly methods available for BCP self-assembly. Finally, the sizes of nanocomponents are independently tunable without influencing the pattern periodicity.

RESULTS AND DISCUSSION

Figure 1A illustrates our multicomponent nanopatterning procedure. In the first level self-assembly, asymmetric polystyrene-*block*-poly(4-vinylpyridine) (PS-*b*-P4VP) BCP thin films were deposited onto a substrate. The subsequent solvent annealing induced P4VP nanocylinder array, whose orientation was controllable by solvent vapor and annealing time.[29−32] Tetrahydrofuran (THF) vapor treatment typically generated monolayer nanocylinders oriented parallel to the substrate (Figure 1B).[30] We note that a prolonged annealing could induce the transition of BCP morphology from parallel to perpendicular cylinder orientation. However, this transition takes several hours, which affords sufficient time to select desired parallel orientation.[31] The BCP thin film was then immersed in an acidic aqueous solution of metal precursor, where anionic metal precursors were specifically associated with the protonated pyridinic nitrogen in P4VP nanocylinders.[32−34] Oxygen plasma etching over the entire area selectively removed the organic components, while leaving the metal nanowire array at the locations of the P4VP cylinders. Figure 1C shows the resultant Pt nanowire array (34 nm period and 10 nm width), prepared from an aqueous solution of Na_2PtCl_4. After this first self-assembly cycle, the second BCP layer was overlaid on the Pt nanowire pattern by spin casting and annealed under THF/toluene mixture vapor. The mixture vapor induced vertical nanocylinders,[29] accurately registered between Pt nanowires (Figure 1D). This vertical nanocylinder morphology is permanently stable regardless of annealing time. The subsequent pattern transfer with Na_2PdCl_4 aqueous solution achieved the multicomponent nanopattern of Pd nanodot arrays alternated with Pt nanowires (Figure 1E). Figure 1F shows the energy-dispersive X-ray spectroscopy (EDS) element mapping results. The Pt component in the nanowires clearly contrasts with the Pd component in the nanodots (Supporting Information, Figure S1). A simple exchange of the metal precursor loading sequence resulted in the multicomponent nanopattern

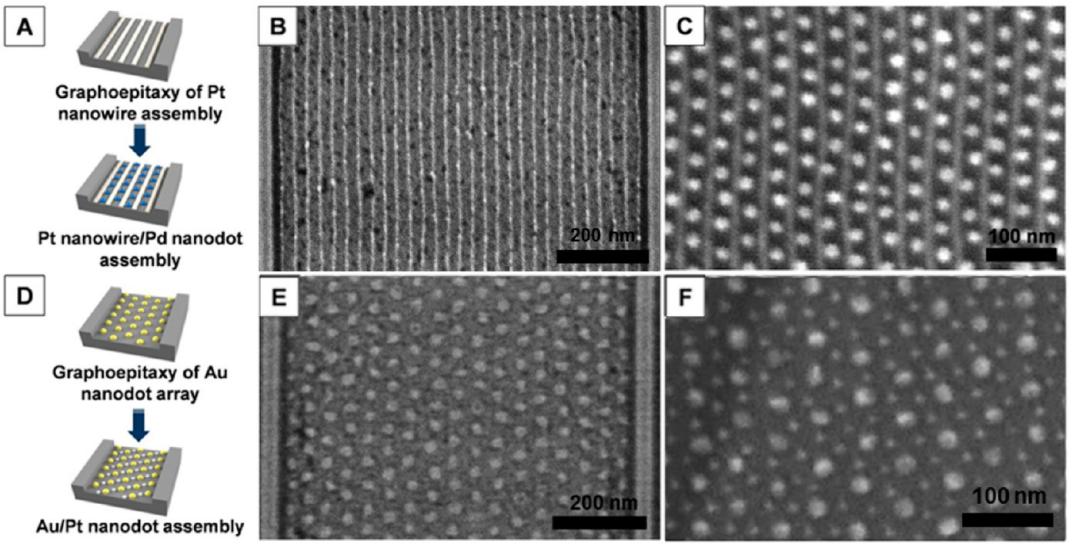

Figure 2. (A and D) Schematic procedure of directed self-assembly by two step process. Laterally ordered nanopatterns of (B) Pt nanowire array, (C) Pt nanowire−Pd nanodot array, (E) Au nanodot array, and (F) Au−Pt nanodot array.

of Pd nanowires and Pt nanodots (Figure 1G, Supporting Information, Figures S1 and S2).

The controllability of nanocylinder orientation with solvent vapor could diversify the attainable nanopatterns. Figure 1H shows a Pt−Pd nanowire assembly achieved from the two self-assembly cycles with THF vapor treatments. The width of nanowires for each metallic component was independently tunable with the concentration and the loading time of the metal precursor solutions (Pt nanowires, 10 nm; Pd nanowires, 8 nm in Figure 1H). Figure 1I presents the Au−Pt binary nanodot array achieved *via* the two self-assembly cycles with mixture vapor treatments. Owing to the various available ionic metal complexes, multicomponent nanopatterns can incorporate a broad spectrum of metallic elements (Supporting Information, Figures S3 and S4). Additionally, other BCPs can be employed for multilevel process, including widely used polystyrene-*block*-poly(methyl methacrylate) (PS-*b*-PMMA), which generally self-assembles *via* thermal annealing rather than solvent annealing (Supporting Information, Figure S5).

Our multicomponent nanopatterning is compatible with various directed self-assembly methods exploiting chemically or topographically prepatterned surfaces.[13,14,35−37] It is noteworthy that directed self-assembly has been employed to create laterally ordered parallel line or hexagonal nanodot patterns in block copolymer thin films *via* solvent annealing as well as thermal annealing.[15,24] In this work, directed self-assembly enabled the controllability of the orientation and lateral ordering of multicomponent nanopatterns. Figure 2 presents multicomponent nanopatterns directed by graphoepitaxy employing topographically prepatterned substrates.[23,27] The nanodomain ordering of the first self-assembly was directed by the graphoepitaxy effect from the topographically prepatterned substrates (Figures2B,E). Solvent annealing of PS-*b*-P4VP thin films within topographic trenches and subsequent metallization generated aligned Pt nanowire arrays (Figure 2B) or hexagonal Au nanodot arrays (Figure 2E). The second self-assembly of the overlaid PS-*b*-P4VP thin films was registered by the bottom metal nanowire or nanodot array generated in the first self-assembly step (Figure 2C,F). Final pattern transfer by metallization generated graphoepitaxially ordered multicomponent nanopatterns of Pd nanodot arrays alternated with Pt nanowires (Figure 2C) or Pt−Au binary nanodot array (Figure 2F). Such self-registration behavior can be further exploited for the laterally ordered multicomponent nanopatterns over a large-area in conjunction with various directed self-assembly approaches.[13,14,20−28]

The chemical composition and the characteristic dimension of nanocomponents generated in the first self-assembly cycle play significant roles for the subsequent registration of the second overlaid self-assembly (Supporting Information, Figures S6 and S7, Figure 3). When thin Pt nanowires with 4.2-nm height and 6.5 nm width were prepared in the first self-assembly, the Pd nanodots from the subsequent step were spontaneously registered along the nanowires (Figure 3A,D). As nanowire became thicker (Figure 3B,C), Pd nanodots gradually migrated into the space between neighboring nanowires (Figure 3E,F). Figure 3G summarizes the variation of wire-dot spacing and the corresponding interdot spacing. In contrast to the morphology evolution with Pt nanowires, when Au nanowires were prepared in the first self-assembly, Pd nanodots were located in the space between nanowires regardless of Au nanowire dimension (Supporting Information, Figure S8).

The interesting morphology variation was analyzed with self-consistent field theory (SCFT) calculation.[38,39]

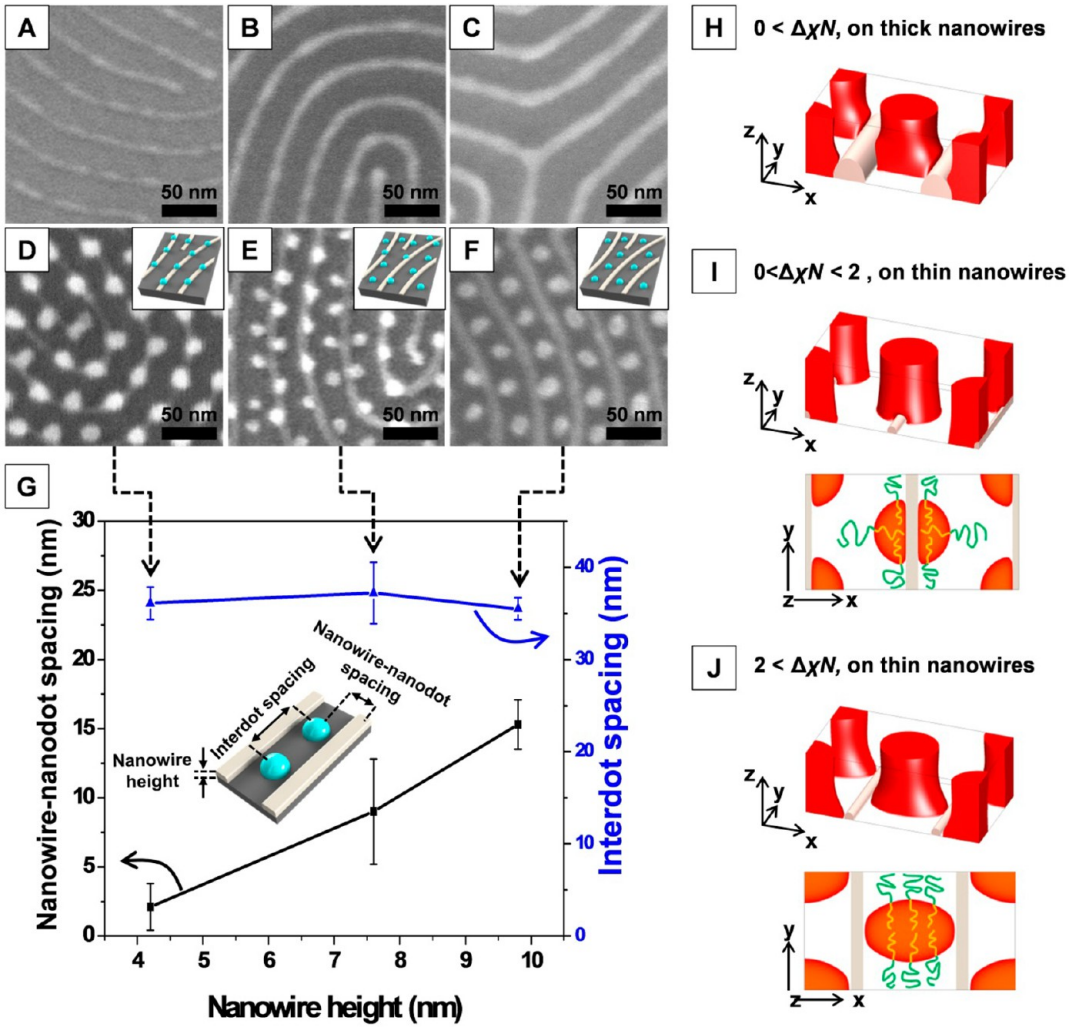

Figure 3. (A–C) SEM images of Pt nanowires with various heights and (D–F) corresponding Pd nanodot registration. (G) Wire-dot spacing and interdot spacing plotted against the nanowire height. (H–J) SCFT calculation of the BCP thin film self-assembled on substrates with parallel nanowires. (H) Vertical cylinders assembled in the space between 'thick' nanowires ($0 < \Delta\chi N$). (I) Vertical cylinders assembled on 'thin' nanowires ($\Delta\chi N < 2$). (J) Vertical cylinders located in the space between 'thin' nanowires ($2 < \Delta\chi N$). If $0 < \Delta\chi N < 2$, vertical cylinders migrate from the top of nanowires to the space between nanowires with nanowire thickness.

The PS-*b*-P4VP BCPs were modeled as AB Gaussian chains with $\chi_{AB}N = 25$ and A (P4VP) fraction of $f = 0.3$, where χ_{AB} is the Flory–Huggins interaction parameter and N is the number of segments in a polymer chain. When this asymmetric BCPs self-assembled into cylinder monolayer oriented parallel to the substrate, the center-to-center distance between neighboring cylinders was calculated to be $L_0 = 1.64aN^{1/2}$ (34 nm in experiment), where a is the statistical segment length. We calculated the equilibrium morphology of the $0.73L_0$ (25 nm)-thick BCP films on the substrate with parallel nanowire array, whose period was consistent to L_0. The bottom Si substrate was assumed to be weakly preferential for P4VP block. We used two different half-elliptical shapes of the surface nanowires (taken from the nanowire dimensions measured in the experiment), whose lateral widths were $0.12L_0$ and $0.37L_0$, and heights were $0.091L$, and $0.27L_0$, respectively. The nanowires were assumed to be filled with immobilized C homopolymers, and the balance of nanowire–polymer interfacial interaction was controlled by interaction contrast, $\Delta\chi N = \chi_{AC}N - \chi_{BC}N$ (see Methods section for details).

SCFT simulation presented that given the bottom surface weakly preferential for P4VP, the registration of P4VP cylinder is dominated by $\Delta\chi N$. If nanowires preferred P4VP ($\Delta\chi N < 0$), P4VP cylinders were registered on the nanowires (Supporting Information, Figure S9), In contrast, if nanowires strongly preferred PS ($\Delta\chi N > 2$), cylinders were registered in the space between nanowires, as observed in the experimental results with Au nanowires (Figure 3H,J, and Supporting Information, Figure S10). An exception was observed when nanowires are thin and weakly preferred PS ($0 < \Delta\chi N < 2$), which corresponds to the case with thin Pt nanowires in the experiments (Figure 3H,I). A close

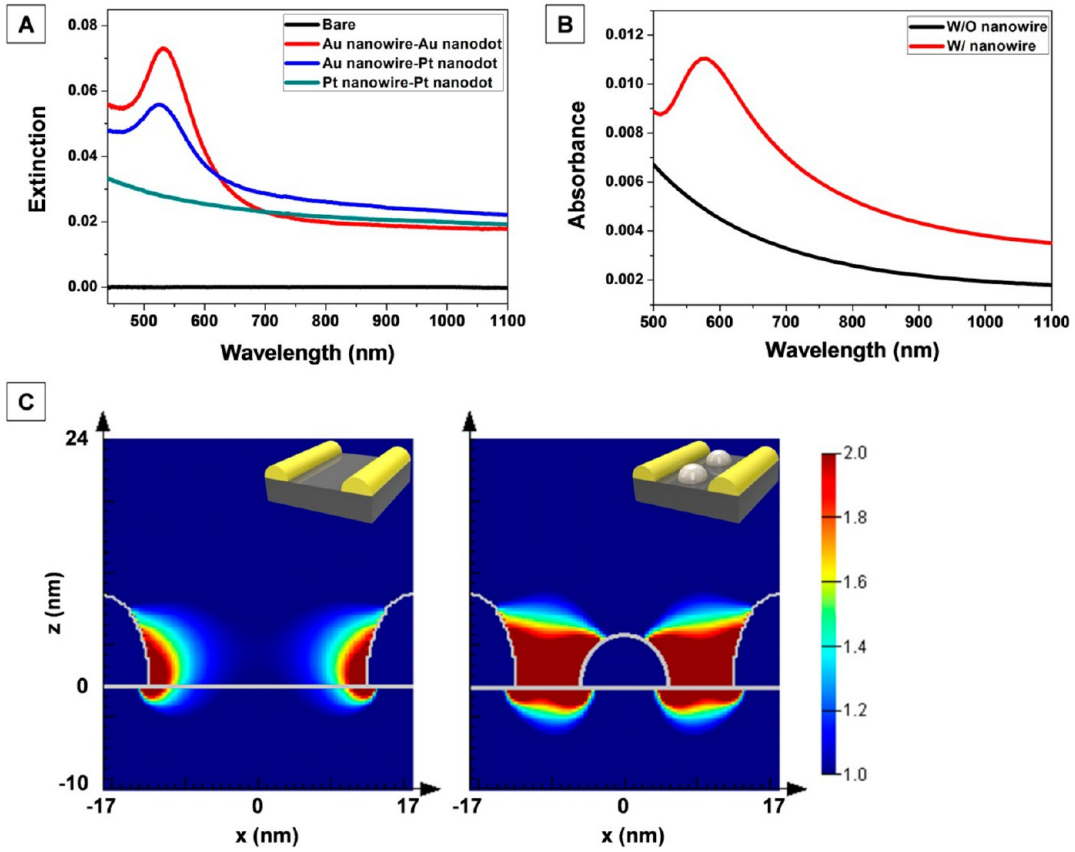

Figure 4. (A) Extinction spectra of various metal nanowire−nanodot arrays. (B) FDTD calculation of light energy absorption at Pt nanodots with or without Au nanowires. (C) The simulated localized electric field intensities normalized with excitation plane wave. Right panel shows the feeding of intensified field into Pt nanodots.

observation of Figure 3I reveals that the bottom part of vertical P4VP cylinders are significantly deformed when cylinders are registered between nanowires. This distortion is caused by the preferential alignment of polymer chains enforced by neighboring bottom nanowires. Since this distortion accompanies the enthalpy penalty arising from the increased cylinder surface area along with the entropy penalty from polymer chain alignment, it is avoided particularly when $\Delta\chi N$ is insufficiently large and nanowires are thin. The effect from $\Delta\chi N$, which weakly prefers PS, could be overcome such that P4VP cylinders are registered along the thin nanowires. As the nanowires became thicker, the P4VP cylinders eventually migrated into the space between nanowires due to the additional enthalpy gain from the enlarged nanowire−PS interfacial area (Figure 3H).

The ability to incorporate multicomponents into a nanopattern offers diverse opportunities in terms of applications. For a photonic application, one component may be designed to serve as an "optical antenna" that efficiently converts incoming optical energy into localized and intensified electromagnetic fields, while another component can act as a localized hotspot or "photon sink". Alternating Au nanowire−Pt nanodot array is a good candidate for such a system. In near-infrared (IR) and visible wavelengths longer than 600 nm, Au with a relatively small imaginary part of electric permittivity can be used as an optical antenna, whereas Pt is a good absorber with a large imaginary permittivity.

Figure 4A shows the experimental extinction spectra of multicomponent nanopatterns over visible and IR wavelengths. In contrast to the Au-only or Pt-only array, the combination of Au nanowire−Pt nanodot array exhibited the highest degree of extinction in the broad wavelength range from 620 to 1100 nm. The synergistic interplay between distinct metallic components led to the extinction largely improved from the average of Au-only and Pt-only arrays. A numerical analysis based on a finite-difference time-domain scheme (Figure 4B) provided light absorption at the nanodots selectively, excluding the absorption at the nanowires.[40,41] The greatly enhanced absorption in the presence of nanowires was caused by the intensified local fields from the nanowires. In Figure 4C, the left panel illustrates the localized electric field intensity in the proximity of nanowires, while the right panel shows the intensified fields feeding of Pt nanodots. Similar synergistic plasmonic effect can be utilized in applications other than simple light absorption, such as sensors, photocatalysis and solar energy utilization, where light functions as an energy or excitation source.[42−44]

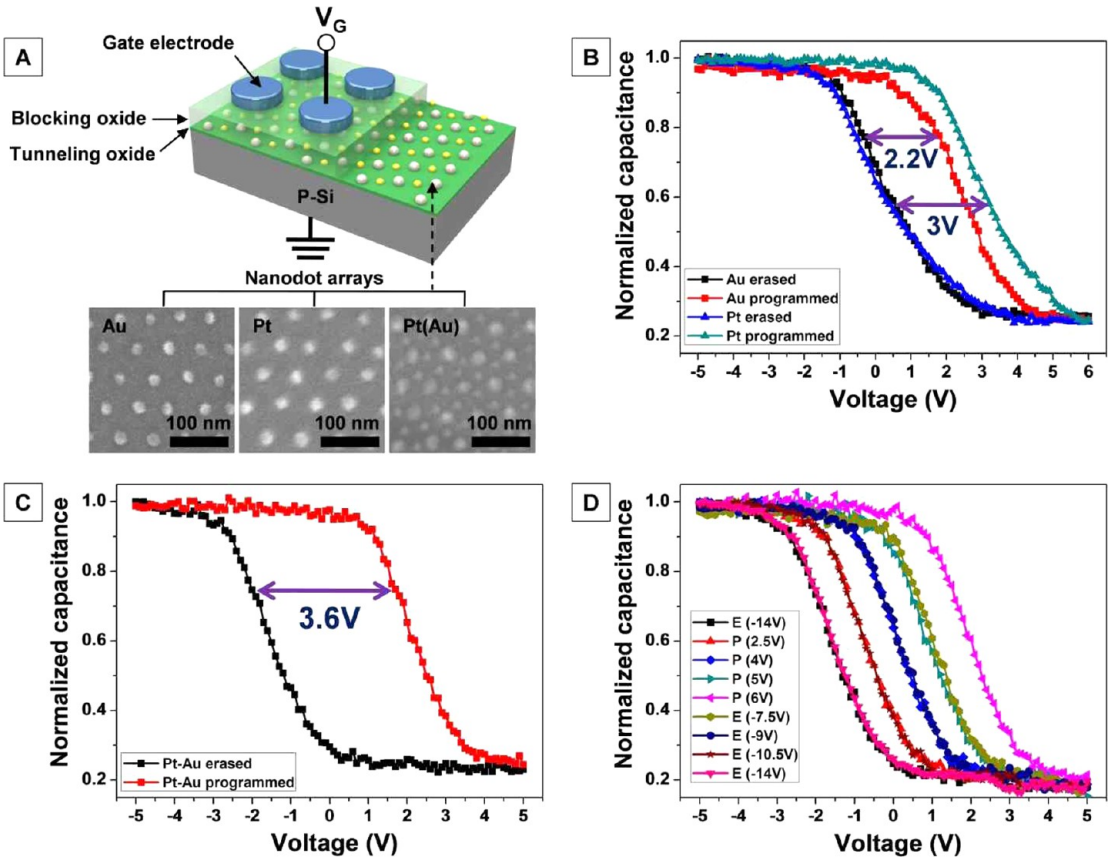

Figure 5. (A) Schematic illustration of charge trap memory device structure. Capacitance−voltage responses of the devices with (B) Pt or Au nanodot array and (C) Pt−Au binary nanodot array. (D) Multilevel data storage capacity of the device with Pt−Au binary nanodot array.

We demonstrate another potential application of multicomponent nanopatterns, where binary nanodot array was employed as charge-trapping layer for nonvolatile flash memory. Presently, widely used film type floating gate frequently suffers from charge leakage, which is a significant bottleneck for the further downscaling of the memory cell dimension. Charge trap layer consisting of discrete metal nanodot array may address such an inherent limitation.[45,46] To date, there have been several reports that utilize the metal nanostructures for charge trap memory devices.[47,48] While those works successfully introduced the charge trapping layers based on metal nanostructures, their processes revealed significant limitations for the scalability to large-area and compatibility with industrial process. By contrast, our work provides a well-established route to overcome such limitations. In addition, memory window could be controlled over a wide range with a precise tunability by employing a variety of multicomponent combinations.

Figure 5A schematically illustrates the device architecture, where single or multiple nanodot array was generated on the 3-nm-thick Al_2O_3 tunneling oxide as a charge trapping layer. The capacitance−voltage responses of the memory devices are plotted in Figure 5B,C upon programming/erasing operation at 1 MHz. The programmed and erased states were switched by applying bias pulses of 7 V for 50 ms and −13 V for 30 ms at the top gate electrodes, respectively. The Pt nanodot device showed a memory window (3.0 V) larger than that of the Au nanodot device (2.2 V) due to the different potential well depths determined by the workfunction and nanodot size.[49]

In contrast, the Pt−Au binary nanodot device showed a greatly increased memory window of 3.6 V (Figure 5C). A higher spatial density of Pt−Au binary nanodot optimized the charge storage capacity and allowed such a larger memory window for charge trap memory. Figure 5D shows the multilevel data storage capacity of the Pt−Au binary nanodot device. The large memory window stabilized five distinguished data states with a proper memory window step (~0.8 V). The uniform distribution and relatively large separation of nanodots (>10 nm) hinder interparticular charge leakage and stabilize the memory operation. Precise tunability of charge trap characteristics was achieved with the combination of nanopatterned multimetallic elements.

CONCLUSIONS

We have demonstrated that BCP self-assembly can create self-registered multicomponent nanopatterns consisting of metal nanowires and nanodots. Directed

self-assembly can create laterally ordered multicomponent nanopatterns, which is hardly attainable by complex colloidal assembly. Significantly, the potential applications of multicomponent nanopattern have been successfully demonstrated for multilevel switching charge trap memory devices and synergistic plasmonic properties. This multicomponent nanopatterning relying on the multilevel self-assembly manifests how to extend periodic molecular self-assembly for diverse pattern shapes, characteristic dimensions, and chemical compositions effectively. The realized synergistic properties, which surpass the simple additive characteristics of constituting nanocomponents, hold great promise for various applications demanding complex architectures with multifunctionalities. Further advance of this approach to integrate semiconductors and other functionalities would greatly strengthen the potential of self-assembled nanopatterning.

METHODS

Materials. Asymmetric block copolymers (BCPs), polystyrene-*block*-poly(4-vinylpyridine)s (PS-*b*-P4VPs, M_n: 24 kg/mol for PS, 9.5 kg/mol for P4VP and 41.5 kg/mol for PS, 17.5 kg/mol for P4VP) were purchased from Polymer Source, Inc. $Na_2PtCl_4 \cdot H_2O$, $Na_2PdCl_4 \cdot 3H_2O$, $HAuCl_4$, $K_3Fe(CN)_6$, and $K_3Co(CN)_6$ were purchased from Strem Chemicals.

Preparation of Multicomponent Nanopatterns. The silicon wafers were immersed in a piranha solution (7:3 mixture of H_2SO_4 and H_2O_2) for 1 h at 110 °C and then washed several times with deionized water. PS-*b*-P4VP BCPs (0.5 wt %) were dissolved in toluene/THF solvent mixtures (80/20, v/v). To fabricate the multicomponent assembly, the first level BCP self-assembly began with 30-nm thick PS-*b*-P4VP thin films spin-coated from a 0.5 wt % toluene/THF solution onto cleaned silicon wafers. The as-spun film was solvent-annealed in a small closed vessel. A homogeneous liquid mixture of THF/hexane (70/30 v/v) or THF/toluene (80/20 v/v) was then injected into the vessel. The small vessel was saturated with the spontaneously evaporated solvent vapor in several minutes at room temperature (25 ± 2 °C). The as-spun films were then annealed for 1−5 h to develop the highly ordered cylindrical nanodomains. The solvent-annealed samples were then immersed in an HCl (aq) solution of a metal ion complex at a desired concentration for a given loading time. After metal ion loading, the samples were rinsed with deionized water several times to remove excess amounts of metal ions and were dried with N_2 gas. An oxygen plasma treatment removed the polymer template and left the metal nanopatterned structures on the silicon substrate. For the second level of BCP self-assembly, PS-*b*-P4VP BCP thin film with a thickness of 30 nm was spin-coated from a 0.5 wt % toluene/THF solution onto metal nanopatterned surfaces. Solvent annealing was then carried out under THF/hexane vapor for in-plane cylinder arrays, or THF/toluene vapor was used for out-of-plane cylinder arrays. After an oxygen plasma treatment following the second metal loading step, a variety of multicomponent assemblies including nanowire−nanodots, nanowire−nanowires and nanodot−nanodot assemblies were obtained.

Fabrication of Silicon Trench. A negative-tone photoresist of SU8 (MicroChem Corp. US) was used to prepare the topographic photoresist confinements. A 180 nm-thick photoresist layer was spin-coated onto a cleaned silicon substrate and soft baked at 65 °C for 20 s. The photoresist film was exposed to an I-line source (Midas/MDA-6000 DUV, KR; wavelength: 365 nm; 9.5 mW/cm^2) through a pattern mask and post baked at 110 °C for 60 s to cross-link the exposed portion of the film selectively. The pattern development process was performed by immersing the exposed photoresist film into a propylene glycol methyl ether acetate (PGMEA) solution for 60 s. Trench patterns with a depth 40 nm were fabrication by SF_6 reactive ion etching.

Fabrication of Charge Trap Memory. The p-type Si (100) substrates were cleaned by a piranha solution (4:1 mixture of H_2SO_4 and H_2O_2) at 150 °C and then dipped into a buffered oxide etchant (BOE) to remove any residual native oxide. An Al_2O_3 tunneling oxide (3 nm) layer was deposited on the Si substrates by atomic layer deposition (ALD) and then a multimetal assembly was prepared using multistep, self-registering BCP self-assembly. Next, a 19-nm Al_2O_3 blocking oxide layer was deposited *via* ALD under the same conditions used for the tunneling oxide layer and 5 nm/100 nm Ti/Pt layers were deposited by reactive radiofrequency magnetron sputtering. The lift-off process was performed to define the round Ti/Pt gate electrodes.

Characterization. The nanoscale morphology of the BCP thin films and metal nanopatterned surfaces was characterized using a Hitachi S-4800 FE-SEM. STEM characterization was performed using a JEOL JEM-ARM200F equipped with an EDS detector. XPS measurements were performed using ESCA 2000 system (Thermo VG Scientific). The height profiles of the metal nanopatterns were analyzed by AFM (Park System, Korea). The UV−vis extinction spectrum of the metal nanopatterns was measured using a UV−vis spectrophotometer (Jasco, V-530). The capacitance−voltage curves of the charge trap memory were measured at 1 MHz by a HP 4194A impedance/gain-phase analyzer at room temperature. The conduction properties were measured using a Keithley 4200-SCS semiconductor characterization system at room temperature.

Self-Consistent Field Theory (SCFT) Calculation. The statistics of the AB BCPs were calculated by the standard SCFT method with modifications given below. To exclude the BCPs from the interior of bottom nanowires, C homopolymers with the same length N were introduced, which were confined within the nanowires due to large external fields (w^{ext} = 50 inside the nanowires).[50] This method guaranteed that the BCP domains have a smooth density transition, and it also allowed us to contrast the A block−nanowire interaction and B block−nanowire interaction by modifying $\chi_{BC}N$ value from 21 to 27, while maintaining $\chi_{AC}N$ = 25. The weak preference of bottom substrate (silicon substrate in our experiments) to P4VP domain was assigned by setting η = 0.1 in the following self-consistency equation:

$$\begin{aligned} w_A(\mathbf{r}) &= -2\eta\delta(z)aN^{1/2} + \chi_{AB}N\phi_B(\mathbf{r}) + \chi_{AC}N\phi_C(\mathbf{r}) + \xi(\mathbf{r}) \\ w_B(\mathbf{r}) &= \chi_{AB}N\phi_A(\mathbf{r}) + \chi_{BC}N\phi_C(\mathbf{r}) + \xi(\mathbf{r}) \\ w_C(\mathbf{r}) &= \chi_{AC}N\phi_A(\mathbf{r}) + \chi_{BC}N\phi_B(\mathbf{r}) + \xi(\mathbf{r}) + w^{ext}(\mathbf{r}) \end{aligned}$$

where $\phi_i(\mathbf{r})$ is the segment density of i type polymers, and $w_i(\mathbf{r})$ is the field acting on it. The simulation box consisted of 3-dimensional 128 × 128 × 128 grid, and the modified diffusion equation for the partition functions of BCPs and homopolymers were solved using the pseudospectral method.[51,52] For both BCPs and homopolymers, 100 mesh points were used in the polymer length direction. The Neumann boundary condition was used for all boundaries to correctly simulate the hexagonal geometry while minimizing the unit cell size. For the first level nanopatterning, we assumed thinnest cylindrical monolayers were self-assembled, which suggested that the nanowire period was $1.64aN^{1/2}$. Because of the substrate pattern, the morphology of the second level nanopatterning deviated from that of the hexagonal cylinder phase; hence, we varied the system size in y direction until minimum free energy was achieved. To find the equilibrium morphology, we basically tested two competing morphologies, one with vertical cylinders on top of the nanowires and the other with vertical cylinders in between the nanowires. As expected, P4VP cylinders preferring nanowires ($\Delta\chi N < 0$) stood on top of the nanowires regardless of the nanowire size (Figure S7). It is also natural that when P4VP cylinders have strong repulsion with nanowires, $\Delta\chi N > 2$, they migrate into the gap between nanowires (Figure S8). The nonintuitive experimental results for Pt were reproducible in the range, $0 < \Delta\chi N < 2$. In this case, the contact

of Pt and P4VP imposes some enthalpic penalty, but the entropy and enthalpy gain described in the main text makes this morphology preferable, only for the thin nanowire case.

Finite-Difference Time-Domain (FDTD) Calculation. A finite difference time-domain method was adopted for the numerical investigation of the optical properties of the metallic nanostructures.[53] It utilized Yee's discretization scheme, and its accuracy and convergence conditions are well understood.[54] The optical properties of the Au and Pt were taken from tabulated values[55] and approximated with analytic functions. The domain of the simulation had the same lateral sizes as the periods of the fabricated sample, and the periodic boundary condition was utilized.[54] The vertical size was 200 nm, as terminated by perfectly matched layers. The computational domain was discretized in 0.25 nm steps inside the metal regions and in progressively larger steps away from the metallic structures, with a maximum step size of 34 nm. Mirror symmetries were exploited to reduce the computation domain by 2- or 4-fold when possible.

Conflict of Interest: The authors declare no competing financial interest.

Acknowledgment. This work was financially supported by Institute for Basic Science (IBS), the Smart IT Convergence System Research Center (Global Frontier project, 2011-0031852) and the National Research Foundation of Korea (NRF) grant (No. 2012R1A1A2043633 and 2012M3A7B4035327) funded by Korean government (MSIP).

Supporting Information Available: STEM images of multicomponent nanopattern with elemental mapping; quantitative analysis of metallic nature of Pt nanowire−Pd nanodot multicomponent nanopattern; Broad field SEM images of multicomponent nanopattern; multicomponent nanopattern achieved with PS-*b*-PMMA thin film, self-assembled via thermal annealing; SCFT calculation of the self-assembled PS-*b*-P4VP thin film morphologies on the substrate with thin and thick metal nanowires having preferred wetting for P4VP or for PS matrix. This material is available free of charge *via* the Internet at http://pubs.acs.org.

REFERENCES AND NOTES

1. Dong, A.; Chen, J.; Vora, P. M.; Kikkawa, J. M.; Murray, C. B. Binary Nanocrystal Superlattice Membranes Self-Assembled at the Liquid−Air Interface. *Nature* **2011**, *466*, 474–477.
2. Leunissen, M. E.; Christova, C. G.; Hynninen, A, -P.; Royall, C. P.; Campbell, A. I.; Imhof, A.; Dijkstra, M.; Roij, R.; Blaaderen, A. Ionic Colloidal Crystals of Oppositely Charged Particles. *Nature* **2005**, *437*, 235–240.
3. Shevchenko, E. V.; Talapin, D. V.; Kotov, N. A.; O'Brien, S.; Murray, C. B. Structural Diversity in Binary Nanoparticle Superlattices. *Nature* **2006**, *439*, 55–59.
4. Sacanna, S.; Irvine, W. T. M.; Chaikin, P. M.; Pine, D. J. Lock and Key Colloids. *Nature* **2010**, *464*, 575–578.
5. Macfarlane, R. J.; Lee, B.; Jones, M. R.; Harris, N.; Schatz, G. C.; Mirkin, C. A. Nanoparticle Superlattice Engineering with DNA. *Science* **2011**, *334*, 204–208.
6. Xia, Y.; Nguyen, T. D.; Yang, M.; Lee, B.; Santos, A.; Paul, P.; Tang, Z.; Glotzer, S. C.; Kotov, N. A. Self-Assembly of Self-Limiting Monodisperse Superparticles from Polydisperse Nanoparticles. *Nat. Nanotechnol.* **2012**, *6*, 580–587.
7. Wang, Y.; Wang, Y.; Breed, D. R.; Manoharan, V. N.; Feng, L.; Hollingsworth, A. D.; Weck, M.; Pine, D. J. Colloids with Valence and Specific Directional Bonding. *Nature* **2012**, *491*, 51–55.
8. Bates, F. S.; Fredrickson, G. H. Block Copolymers-Designer Soft Materials. *Phys. Today* **1999**, *52*, 32–38.
9. Park, M.; Harrison, C.; Chaikin, P. M.; Register, R. A.; Adamson, D. H. Block Copolymer Lithography: Periodic Arrays of $\sim 10^{11}$ Holes in 1 Square Centimeter. *Science* **1997**, *276*, 1401–1404.
10. Thurn-Albrecht, T.; Schotter, J.; Kastle, C. A.; Emley, N.; Shibauchi, T.; Krusin-Elbaum, L.; Guarini, K.; Black, C. T.; Tuominen, M. T.; Russell, T. P. Ultrahigh-Density Nanowire Arrays Grown in Self-Assembled Diblock Copolymer Templates. *Science* **2000**, *290*, 2126–2129.
11. Segalman, R. A.; Yokoyama, H.; Kramer, E. J. Graphoepitaxy of Spherical Domain Block Copolymer Films. *Adv. Mater.* **2001**, *13*, 1152–1155.
12. Ludwigs, S.; Boker, A.; Voronov, A.; Rehse, N.; Magerle, R.; Karusch, G. Self-Assembly of Functional Nanostructures from ABC Triblock Copolymers. *Nat. Mater.* **2003**, *2*, 744–747.
13. Kim, S. O.; Solak, H. H.; Stoykovich, M. P.; Ferrier, N. J.; de Pablo, J. J.; Nealey, P. F. Epitaxial Self-Assembly of Block Copolymers on Lithographically Defined Nanopatterned Substrates. *Nature* **2003**, *424*, 411–414.
14. Stoykovich, M. P.; Muller, M.; Kim, S. O.; Solak, H. H.; Edwards, E. W.; de Pablo, J. J.; Nealey, P. F. Directed Assembly of Block Copolymer Blends into Nonregular Device-Oriented Structures. *Science* **2005**, *308*, 1442–1446.
15. Chai, J.; Wang, D.; Fan, X. N.; Buriak, J. M. Assembly of Aligned Linear Metallic Patterns on Silicon. *Nat. Nanotechnol.* **2007**, *2*, 500–506.
16. Tang, C.; Lennon, E. M.; Fredrickson, G. H.; Kramer, E. J.; Hawker, C. J. Evolution of Block Copolymer Lithography to Highly Ordered Square Arrays. *Science* **2008**, *322*, 429–432.
17. Jeong, S.-J.; Xia, G. D.; Kim, B. H.; Shin, D. O.; Kwon, S.-H.; Kang, S.-W.; Kim, S. O. Universal Block Copolymer Lithography for Metals, Semiconductors, Ceramics, and Polymers. *Adv. Mater.* **2008**, *20*, 1898–1904.
18. Park, S.; Lee, D. H.; Xu, J.; Kim, B.; Hong, S. W.; Jeong, U.; Xu, T.; Russell, T. P. Macroscopic 10-Terabit-Per-Square-Inch Arrays from Block Copolymers with Lateral Order. *Science* **2009**, *323*, 1030–1033.
19. Arora, H.; Du, P.; Tan, K. W.; Hyun, J. K.; Grazul, J.; Xin, H. L.; Muller, D. A.; Thompson, M. O.; Wiesner, U. Block Copolymer Self-Assembly-Directed Single-Crystal Homo- and Heteroepitaxial Nanostructures. *Science* **2010**, *330*, 214–219.
20. Hong, S. W.; Huh, J.; Gu, X. D.; Lee, D. H.; Jo, W. H.; Park, S.; Xu, T.; Russell, T. P. Unidirectionally Aligned Line Patterns Driven by Entropic Effects on Faceted Surfaces. *Proc. Natl. Acad. Sci. U.S.A.* **2012**, *109*, 1420–1406.
21. Kim, S. O.; Kim, B. H.; Meng, D.; Shin, D. O.; Koo, C. M.; Solak, H. H.; Wang, Q. Novel Complex Nanostructure from Directed Assembly of Block Copolymers on Incommensurate Surface Patterns. *Adv. Mater.* **2007**, *19*, 3271–3275.
22. Ruiz, R.; Kang, H. M.; Detcheverry, F. A.; Dobisz, E.; Kercher, D. S.; Albrecht, T. R.; de Pablo, J. J.; Nealey, P. F. Density Multiplication and Improved Lithography by Directed Block Copolymer Assembly. *Science* **2008**, *321*, 936–939.
23. Bita, I.; Yang, J. K. W.; Jung, Y. S.; Ross, C. A.; Thomas, E. L.; Berggren, K. K. Graphoepitaxy of Self-Assembled Block Copolymers on Two-Dimensional Periodic Patterned Templates. *Science* **2008**, *321*, 939–943.
24. Jeong, S.-J.; Kim, J. E.; Moon, H. S.; Kim, B. H.; Kim, S. M.; Kim, J. B.; Kim, S. O. Soft Graphoepitaxy of Block Copolymer Assembly with Disposable Photoresist Confinement. *Nano Lett.* **2009**, *9*, 2300–2305.
25. Park, S. H.; Shin, D. O.; Kim, B. H.; Yoon, D. K.; Kim, K.; Lee, S. Y.; Oh, S.-H.; Choi, S.-W.; Jeon, S. C.; Kim, S. O. Block Copolymer Multiple Patterning Integrated with Conventional ArF Lithography. *Soft Matter* **2010**, *6*, 120–125.
26. Cheng, J. Y.; Sanders, D. P.; Truong, H. D.; Harrer, S.; Friz, A.; Holmes, S.; Colburn, M.; Hinsberg, W. D. Simple and Versatile Methods to Integrate Directed Self-Assembly with Optical Lithography Using a Polarity-Switched Photoresist. *ACS Nano* **2010**, *4*, 4815–4823.
27. Yang, J. K. W.; Jung, Y. S.; Chang, J. B.; Mickiewicz, R. A.; Alexander-Katz, A.; Ross, C. A.; Berggren, K. K. Complex Self-Assembled Patterns using Sparse Commensurate Templates with Locally Varying Motifs. *Nat. Nanotechnol.* **2010**, *5*, 256–260.
28. Tavakkoli, A. K. G.; Gotrik, K. W.; Hannon, A. F.; Alexander-Katz, A.; Ross, C. A.; Berggren, K. K. Templating Three-Dimensional Self-Assembled Structures in Bilayer Block Copolymer Films. *Science* **2012**, *336*, 1294–1298.
29. Park, S.; Wang, J.-Y.; Kim, B.; Chen, W.; Russell, T. P. Solvent-Induced Transitioin from Micelles in Solution to Cylindrical Microdomains in Diblock Copolymer Thin Films. *Macromolecules* **2007**, *40*, 9059–9063.

30. Park, S.; Kim, B.; Cirpan, A.; Russell, T. P. Preparation of Metallic Line Patterns from Functional Block Copolymers. *Small* **2009**, *5*, 1343–1348.
31. Lee, D. H.; Cho, H.; Yoo, S.; Park, S. Ordering Evloution of Block Copolymer Thin Films upon Solvent-Annealing Process. *J. Colloid Interface Sci.* **2012**, *383*, 118–123.
32. Shin, D. O.; Lee, D. H.; Moon, H.-S.; Jeong, S.-J.; Kim, J. Y.; Mun, J. H.; Cho, H.; Park, S.; Kim, S. O. Sub-Nanometer Level Size Tuning of a Monodiisperse Nanoparticle Array *via* Block Copolymer Lithography. *Adv. Funct. Mater.* **2011**, *21*, 250–254.
33. Chai, J.; Buriak, J. M. Using Cylindrical Domains of Block Copolymers to Self-Assemble and Align Metallic Nanowires. *ACS Nano* **2008**, *2*, 489–501.
34. Wu, N. L. Y.; Zhang, X.; Murphy, J. N.; Chai, J.; Harris, K. D.; Buriak, J. M. Density Doubling of Block Copolymer Templated Features. *Nano Lett.* **2012**, *12*, 264–268.
35. Ruiz, R.; Sandstrom, R. L.; Black, C. T. Induced Oritentational Order in Symmetric Diblock Copolymer Thin Films. *Adv. Mater.* **2007**, *19*, 587–591.
36. Son, J. G.; Hannon, A. F.; Gotrik, K. W.; Alexander-Katz, A.; Ross, C. A. Hierarchical Nanostructures by Sequential Self-Assembly of Styrene-Dimethylsiloxane Block Copolymers of Different Periods. *Adv. Mater.* **2011**, *23*, 634–639.
37. Jeong, S.-J.; Moon, H.-S.; Shin, J.; Kim, B. H.; Shin, D. O.; Kim, J. Y.; Lee, Y.-H.; Kim, J. U.; Kim, S. O. One-Dimensional Metal Nanowire Assembly *via* Block Copolymer Soft Graphoepitaxy. *Nano Lett.* **2010**, *10*, 3500–3505.
38. Drolet, F.; Fredrickson, G. H. Combinatorial Screening of Complex Block Copolymer Assembly with Self-Consistent Field Theory. *Phys. Rev. Lett.* **1999**, *83*, 4317–4320.
39. Kim, J. U.; Matsen, M. W. Positioning Janus Nanoparticles in Block Copolymer Scaffolds. *Phys. Rev. Lett.* **2009**, *102*, 078303.
40. Shin, J.; Shen, J.-T.; Fan, S. Three-Dimensional Metamaterials with an Ultra-High Effective Refractive Index over Broad Bandwidth. *Phys. Rev. Lett.* **2009**, *02*, 093903.
41. Choi, M.; Lee, S. H.; Kim, Y.; Kang, S. B.; Shin, J.; Kwak, M. H.; Kang, K,-Y.; Lee, Y.-H.; Park, N.; Min, B. A Terahertz Metamaterial with Unnaturally High Refractive Index. *Nature* **2011**, *470*, 369–373.
42. Atwater, H. A.; Polman, A. Plasmonics for Improved Photovoltaic Devices. *Nat. Mater.* **2010**, *9*, 205–213.
43. Mistark, P. A.; Park, S.; Yalcin, S. E.; Lee, D. H.; Yavuzcetin, O.; Tuominen, M. T.; Russell, T. O; Achermann, M. Block Copolymer-Based Plasmonic Nanostructures. *ACS Nano* **2009**, *3*, 3987–3992.
44. Shin, D. O.; Jeong, J.-R.; Han, T. H.; Koo, C. M.; Park, H.-J.; Lim, Y. T.; Kim, S. O. A Plasmonic Biosensor Array by Block Copolymer Lithography. *J. Mater. Chem.* **2010**, *20*, 7241–7247.
45. Black, C. T.; Ruiz, R.; Breyta, G.; Cheng, J. Y.; Colburn, M. C.; Guarini, K. W.; Kim, H.-C.; Zhang, Y. Q. Polymer Self-Assembly in Semiconductor Microelectronics. *IBM J. Rev. Dev.* **2007**, *51*, 605–633.
46. Lee, J.-W.; Ryu, S. W.; Shin, D. O.; Kim, B. H.; Kim, S. O.; Choi, Y.-K. Geometric Effects of Nanocrystals in Nonvolatile Memory using Block Copolymer Nanotemplate. *Solid-State Electron.* **2009**, *53*, 640–643.
47. Hofmann, R.; Krishna, N. Self-Assembled Metallic Nanocrystal Structures for Advanced Non-Volatile Memory Applications. *Microelectron. Eng.* **2008**, *85*, 1975–1978.
48. Lee, J.-S.; Kim, Y.-M.; Kwon, J.-H.; Shin, H.; Sohn, B.-H.; Lee, J. Tunable Memory Characteristics of Nanostructured, Nonvolatile Charge Trap Memory Devices Based on a Binary Mixture of Metal Nanoparticles as a Charge Trapping Layer. *Adv. Mater.* **2008**, *21*, 178–183.
49. Lee, C.; Meteer, J.; Narayanan, V.; Kan, E. C. Self-Assembly of Metal Nanocrystals on Ultrathin Oxide for Nonvolatile Memory Applications. *J. Electron. Mater.* **2005**, *34*, 1–11.
50. Kim, S.; Shin, D. O.; Choi, D.-G.; Jeong, J.-R.; Mun, J. H.; Yang, Y.-B.; Kim, J. U.; Kim, S. O.; Jeong, J.-H. Graphoepitaxy of Block-Copolymer Self-Assembly Integrated with Single-Step ZnO Nanoimprinting. *Small* **2012**, *8*, 1563–1569.
51. Rasmussen, K. Ø.; Kalosakas, G. Improved Numerical Algorithm for Exploring Block Copolymer Mesophases. *J. Polym. Sci., Part B: Polym. Phys.* **2002**, *40*, 1777–1783.
52. Stasiak, P.; Matsen, M. W. Efficiency of Pseudo-Spectral Algorithms with Anderson Mixing for the SCFT of Periodic Block-Copolymer Phases. *Eur. Phys. J. E* **2011**, *34*, 110.
53. Fan, S.; Villeneuve, P. R.; Joannopoulos, J. D. Large Omnidirectional Band Gaps in Metallodielectric Photonic Crystals. *Phys. Rev. B* **1996**, *54*, 11245.
54. Taflove, A.; Hagness, S. C. *Computational Electrodynamics: The Finite-Di□erence Time-Domain Method*, 3rd ed.; Artech House: Boston, MA, 2005.
55. Palik, E. D. *Handbook of Optical Constants of Solids*; Academic Press: New York, 1997.